Editors' Suggestion

Demonstration of a Nonstoquastic Hamiltonian in Coupled Superconducting Flux Qubits

I. Ozfidan,[1,‡] C. Deng,[1,†,‡] A.Y. Smirnov,[1] T. Lanting,[1] R. Harris,[1] L. Swenson,[1] J. Whittaker,[1] F. Altomare,[1] M. Babcock,[1] C. Baron,[1] A.J. Berkley,[1] K. Boothby,[1] H. Christiani,[1] P. Bunyk,[1] C. Enderud,[1] B. Evert,[1] M. Hager,[1] A. Hajda,[1] J. Hilton,[1] S. Huang,[1] E. Hoskinson,[1] M.W. Johnson,[1] K. Jooya,[1] E. Ladizinsky,[1] N. Ladizinsky,[1] R. Li,[1] A. MacDonald,[1] D. Marsden,[1] G. Marsden,[1] T. Medina,[1] R. Molavi,[1] R. Neufeld,[1] M. Nissen,[1] M. Norouzpour,[1] T. Oh,[1] I. Pavlov,[1] I. Perminov,[1] G. Poulin-Lamarre,[1] M. Reis,[1] T. Prescott,[1] C. Rich,[1] Y. Sato,[1] G. Sterling,[1] N. Tsai,[1] M. Volkmann,[1] W. Wilkinson,[1] J. Yao,[1] and M.H. Amin[1,2,*]

[1] *D-Wave Systems Inc., 3033 Beta Avenue, Burnaby, British Columbia V5G 4M9, Canada*

[2] *Department of Physics, Simon Fraser University, Burnaby, British Columbia V5A 1S6, Canada*

(Received 8 November 2019; revised manuscript received 9 January 2020; accepted 18 February 2020; published 16 March 2020)

Hamiltonian-based quantum computation is a class of quantum algorithms in which the problem is encoded in a Hamiltonian and the evolution is performed by a continuous transformation of the Hamiltonian. Universal adiabatic quantum computing, quantum simulation, and quantum annealing are examples of such algorithms. Up to now, all implementations of this approach have been limited to qubits coupled via a single degree of freedom. This gives rise to a stoquastic Hamiltonian that has no *sign problem* in quantum Monte Carlo simulations. In this paper, we report implementation and measurements of two superconducting flux qubits coupled via two canonically conjugate degrees of freedom—charge and flux—to achieve a nonstoquastic Hamiltonian. We perform microwave spectroscopy to extract circuit parameters and show that the charge coupling manifests itself as a $\sigma^y\sigma^y$ interaction in the computational basis. We observe destructive interference in quantum coherent oscillations between the computational-basis states of the two-qubit system. Finally, we show that the extracted Hamiltonian is nonstoquastic over a wide range of parameters.

DOI: 10.1103/PhysRevApplied.13.034037

I. INTRODUCTION

Early generation processors [1] for Hamiltonian-based quantum computation were designed to perform quantum annealing, a heuristic algorithm for finding low-energy configurations of a system [2–4]. With additional features, other applications such as quantum simulation [5,6] and machine learning [7,8] have become possible. Currently available large-scale quantum processors are made from a network of radio-frequency superconducting quantum-interference devices (rf SQUIDs) [1,9,10]. Interaction between pairs of devices is realized through tunable magnetic coupling of their flux degrees of freedom. The low-energy dynamics of individual rf SQUIDs are effectively captured with their two lowest-energy eigenstates, allowing one to approximate rf SQUIDs as qubits, described by Pauli matrices $\sigma^x, \sigma^y, \sigma^z$. The computational-basis states $|\uparrow\rangle$ and $|\downarrow\rangle$ (eigenfunctions of σ^z) correspond to directions of persistent current in the body of the rf SQUID. This network implements the transverse-field Ising-model Hamiltonian:

$$H = -\frac{1}{2}\sum_i \Delta_i \sigma_i^x + \sum_i h_i \sigma_i^z + \sum_{i<j} J_{ij}\sigma_i^z\sigma_j^z, \quad (1)$$

where Δ_i and h_i are the tunneling amplitude and energy bias of qubit i, respectively, and J_{ij} is the magnetic coupling strength between qubits i and j. Quantum annealing is performed by adjusting $\Delta_i \gg h_i, J_{ij}$ at the beginning of the annealing process and gradual evolution until $\Delta_i \ll h_i, J_{ij}$ at the end.

One important property of Hamiltonian (1) is that it is *stoquastic*. A Hamiltonian is stoquastic if there exists a local basis such that all off-diagonal elements of the Hamiltonian are real and nonpositive [11–13]. A positive off-diagonal element would cause negative transition probabilities, which cannot be simulated by stochastic processes. This issue is called "sign problem" in stochastic algorithms such as quantum Monte Carlo (QMC)

*amin@dwavesys.com

†Present address: Alibaba Quantum Laboratory, Alibaba Group, Hangzhou, China.

‡These authors contributed equally.

algorithms [14], meaning that QMC algorithms cannot simulate equilibrium properties of such a Hamiltonian [15–17]. These algorithms typically operate in a local basis, in which all basis vectors are product states of individual qubits. Otherwise, representation of the basis vectors requires exponential resources. If a Hamiltonian is nonstoquastic, there should exist no local basis in which all off-diagonal elements are negative or zero. For some stoquastic Hamiltonians, finding the local transformation that cures the sign problem is by itself intractable [12]. Therefore, proving that a Hamiltonian is nonstoquastic is also intractable. To achieve nonstoquasticity, additional interactions such as $\sigma_i^x\sigma_j^x$ or $\sigma_i^y\sigma_j^y$ are needed in Hamiltonian (1). Such interactions can enhance the performance of quantum annealing [18,19], extend the range of quantum simulations [20], provide a path toward annealing-based universal quantum computation [21–23], and enable error suppression in quantum annealing [24,25]. Nonstoquasticity may also be achieved via nonadiabatic evolution [26].

II. HAMILTONIAN

To implement a nonstoquastic Hamiltonian, we use two rf SQUIDs coupled both inductively, through a tunable mutual inductance M_{12} [10], and capacitively, through a fixed capacitance C_{12}, as shown in Fig. 1(a).

The Hamiltonian of the system is

$$H = \sum_{i=1}^{2}\left[\frac{Q_i^2}{2\widetilde{C}_i} + \frac{(\Phi_{q,i}-\Phi_{q,i}^x)^2}{2L_i} - E_{Ji}(\Phi_{\mathrm{CJJ},i}^x)\cos\frac{2\pi\Phi_{q,i}}{\Phi_0}\right] + \frac{M_{12}(\Phi_{\mathrm{co}}^x)(\Phi_{q,1}-\Phi_{q,1}^x)(\Phi_{q,2}-\Phi_{q,2}^x)}{L_1L_2} + \frac{C_{12}\,Q_1Q_2}{C_1C_2+(C_1+C_2)C_{12}}, \tag{2}$$

where Q_i and $\Phi_{q,i}$ are charge and flux variables that satisfy the commutation relation $[\Phi_{q,i},Q_j]=i\hbar\,\delta_{ij}$, $\Phi_{q,i}^x$ and $\Phi_{\mathrm{CJJ},i}^x$ are external fluxes, and $\Phi_0=\pi\hbar/e$ is the flux quantum. Each rf SQUID is characterized by its capacitance C_i, inductance L_i, and tunable Josephson energy $E_{Ji}(\Phi_{\mathrm{CJJ},i}^x)\approx(\Phi_0/2\pi)I_{ci}\cos(\pi\Phi_{\mathrm{CJJ},i}^x/\Phi_0)$ [9] (for a more detailed description, see Appendix A 1). The tunable mutual inductance M_{12} is adjusted with the coupler control bias Φ_{co}^x. The renormalized capacitances are defined as $\widetilde{C}_{1(2)}=C_{1(2)}+C_{12}C_{2(1)}/(C_{2(1)}+C_{12})$. Capacitive couping was proposed and analyzed theoretically for flux qubits in Refs. [27–30] and is commonly used in transmon qubits [31,32].

The potential energy of each rf SQUID can have a double-well shape [see the two-qubit potential in Fig. 1(b)]. The barrier height of the potential is controlled by $\Phi_{\mathrm{CJJ},i}^x$, which tunes the tunneling amplitude Δ_i, but also changes the persistent current. The potential is monostable when $\Phi_{\mathrm{CJJ},i}^x=0.5\Phi_0$. The flux bias $\Phi_{q,i}^x$ adjusts the tilt of the potential, setting h_i. Both $\Phi_{q,i}^x$ and $\Phi_{\mathrm{CJJ},i}^x$ are controlled by high-bandwidth coaxial lines, allowing microwave operation and fast quench of the coherent dynamics. At the end of the quench, which involves raising the tunneling barrier rapidly, the persistent current is measured via a shift register coupled to a microwave resonant readout [33,34].

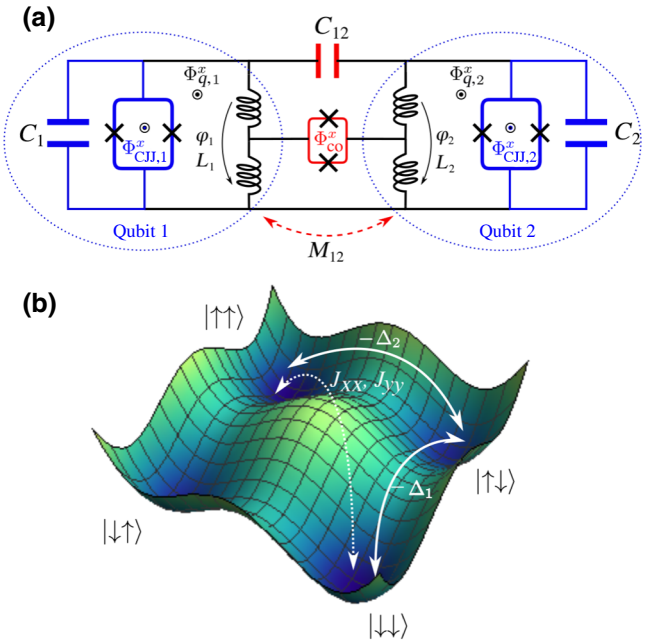

FIG. 1. Schematic and potential energy of coupled rf SQUIDs. (a) Schematic circuit of two rf SQUIDs coupled inductively via a tunable coupler and capacitively via a fixed capacitor. (b) Effective potential energy of the circuit shown in (a). Arrows show tunneling paths between $|\uparrow\uparrow\rangle$ and $|\downarrow\downarrow\rangle$ states within the two-state approximation for each rf SQUID. The solid arrows indicate tunneling due to two consecutive single-qubit flips facilitated by σ_i^x. The dotted arrow represents direct two-qubit cotunneling due to $\sigma_1^x\sigma_2^x$ and $\sigma_1^y\sigma_2^y$. The tunneling amplitudes may have opposite signs, thus leading to destructive interference.

A. Parameter extraction

Before characterizing the circuit parameters, we calibrate the tunable magnetic coupler, which provides the function $M_{12}(\Phi_{\mathrm{co}}^x)$ as discussed in Ref. [10]. For the rest of the paper, we treat the coupler as a simple tunable mutual inductance, assuming the dynamics of the coupler are significantly faster than single-qubit and coupled-qubit dynamics (Born-Oppenheimer approximation). Next we measure the persistent current of each qubit for a range of Φ_{CJJ}^x in a regime where its tunneling amplitude is negligible and the other qubit is kept monostable. We fit these measurements to a classical rf-SQUID model [9] and obtain $I_{c,1}=3.227\ \mu$A, $L_1=231.9$ pH, $I_{c,2}=3.157\ \mu$A, and $L_2=239.0$ pH.

To extract the remainder of the circuit parameters, we perform microwave spectroscopy on the single-qubit and two-qubit systems [35]. Applying a fixed $\Phi^x_{\mathrm{CJJ},2}$ to the second qubit, we sweep the barrier height of the first qubit, controlled by the external flux bias $\Phi^x_{\mathrm{CJJ},1}$. At every $\Phi^x_{\mathrm{CJJ},1}$, a long microwave pulse (1 μs) is applied to the first qubit to excite the two-qubit system. The energy eigenstates are read out by our applying an adiabatic tilt to both qubits to transform the energy eigenstates into persistent-current states, followed by a quench to freeze the dynamics of both qubits before readout. The pulse sequence is shown in Fig. 2(a). The excited-state population of each qubit serves as a signal for detecting the energy spectrum of the coupled system. We collect effective single-qubit data by removing the potential barrier of the other qubit, making it monostable, and perform two-qubit spectroscopy for various $\Phi^x_{\mathrm{CJJ},2}$. In both sets of experiments we keep $\Phi^x_{q,1} = \Phi^x_{q,2} = 0$ and $M_{12} = 0$ pH, while the capacitive coupling is always present. Jointly fitting the effective single-qubit and two-qubit spectroscopy data to the coupled rf-SQUID model, Eq. (2), we obtain the rest of the circuit parameters, $C_1 = 119.5$ fF, $C_2 = 116.4$ fF, and $C_{12} = 132$ fF.

Figures 2(b)–2(d) show two-qubit-spectroscopy data along with the numerical fit obtained with the rf-SQUID model (2). One can see a clear Δ_2-dependent anticrossing that is in good agreement with simulations (solid lines). Without any type of coupling, the spectral lines representing the first excited states of noninteracting qubits would cross as shown by the dashed lines [36]. The anticrossing is therefore a signature of capacitive coupling (at $M_{12} = 0$) and its energy gap is a measure of the coupling strength. The extracted anticrossing gaps of 0.77, 1.14, and 1.78 GHz at $\Delta_2 = 1.5$, 2.0, and 3.0 GHz, respectively, suggest a strong capacitive coupling.

B. Reduction to qubit model

We now reduce the continuous rf-SQUID model to a two-state (qubit) model, which is relevant for quantum computation. Although the continuous Hamiltonian (2) is stoquastic [13], the reduced qubit Hamiltonian will

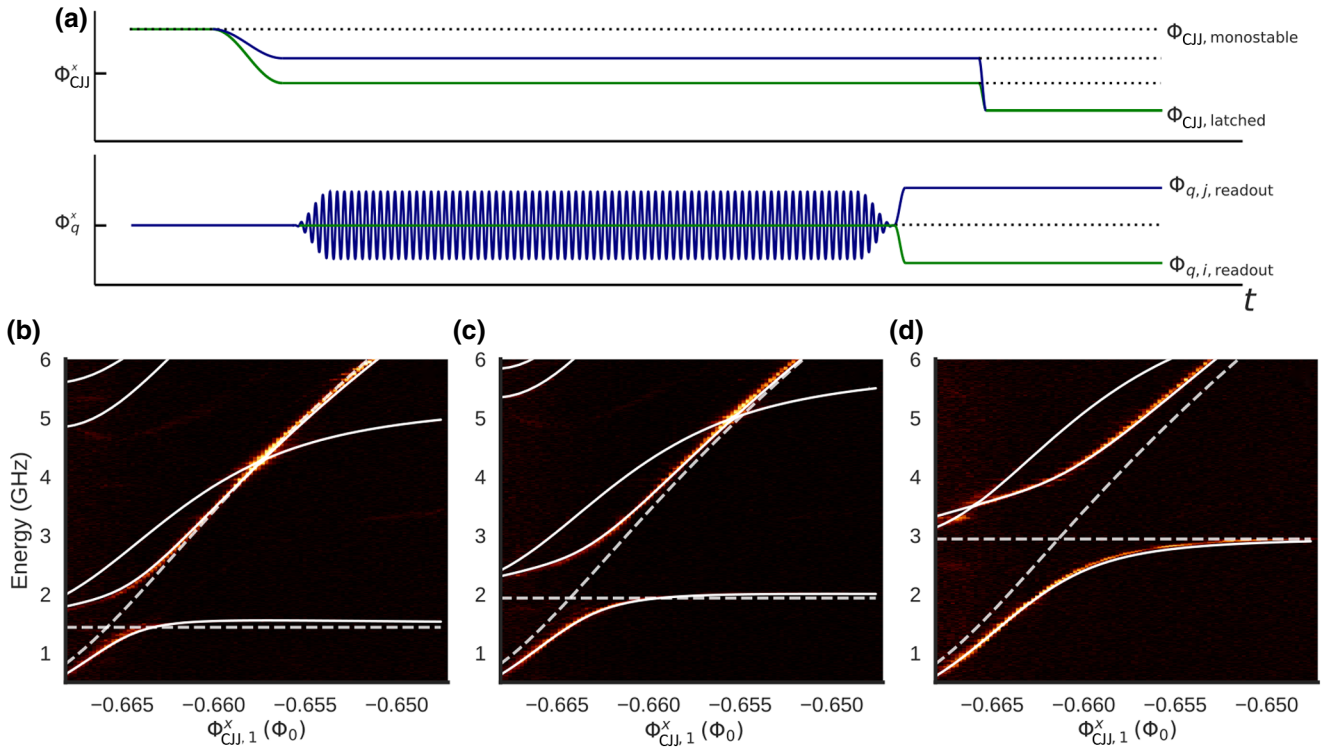

FIG. 2. Microwave spectroscopy of the coupled two-qubit system at $M_{12} = 0$ and $\Phi^x_{q,1} = \Phi^x_{q,2} = 0$. (a) Pulse sequences for two-qubit microwave spectroscopy. At $\Phi_{\mathrm{CJJ,monostable}}$ the tunneling barrier is at its lowest, resulting in a monostable potential. At $\Phi^x_{\mathrm{CJJ,latched}}$ the tunneling barrier is high and the tunneling amplitude is negligible. The effective single-qubit spectroscopy has the same pulse sequence except for $\Phi^x_{\mathrm{CJJ},2} = 0.5\Phi_0$. (b)–(d) Two-qubit-spectroscopy energy versus $\Phi^x_{\mathrm{CJJ},1}$, which controls the qubit-1 barrier height. Qubit 2 is kept at $\Phi^x_{\mathrm{CJJ},2}$, corresponding to effective single-qubit tunneling amplitudes (b) $\Delta_2 = 1.5$ GHz, (c) $\Delta_2 = 2.0$ GHz, and (d) $\Delta_2 = 3.0$ GHz. Energies are measured relative to the ground state. The solid lines are obtained by our fitting the rf-SQUID model, Eq. (2), to the experimental data. Dashed lines represent the excited-state energies of uncoupled qubits ($M_{12} = 0, C_{12} = 0$) given the other fitting parameters.

have nonstoquastic terms. The flux degree of freedom is described by σ_i^z, with $\sigma_1^z\sigma_2^z$ representing the inductive coupling. The charge operator $Q_i = -i\hbar(\partial/\partial\Phi_i)$, on the other hand, is related to σ_i^y since both are complex in the computational basis. Thus, the electrostatic coupling between the rf SQUIDs gives rise to a $\sigma_1^y\sigma_2^y$ interaction. This term describes direct two-qubit cotunneling. In addition, a $\sigma_1^x\sigma_2^x$ term is obtained that reflects cotunneling mediated by the high-energy states of the rf SQUIDs. The effective two-qubit Hamiltonian can be represented as

$$H = -\frac{\Delta_1}{2}\sigma_1^x - \frac{\Delta_2}{2}\sigma_2^x + h_1\sigma_1^z + h_2\sigma_2^z + \sum_{\alpha,\beta} J_{\alpha\beta}\sigma_1^\alpha\sigma_2^\beta, \tag{3}$$

where $\alpha, \beta = \{x, y, z\}$. Since the continuous Hamiltonian (2) is real, the reduced Hamiltonian will also be real in the basis chosen; therefore, $J_{\alpha y} = J_{y\alpha} = 0$ for $\alpha \neq y$. The parameters of Hamiltonian (3) are derived from the rf-SQUID model through a reduction technique described in Appendix A 2. The circuit parameters of the rf-SQUID model are extracted by fitting energy levels calculated using Eq. (2) to experimental data obtained from uncoupled ($M_{12} = 0$) rf SQUIDs.

III. EXPERIMENTAL RESULTS

In this section, we show that the reduced Hamiltonian (3) can explain experimental observations with no further fitting parameters.

A. Microwave spectroscopy

Figures 3(a)–3(c) depict two-qubit spectra at nonzero energy bias ($h_i \neq 0$). The solid white lines correspond to numerical simulations obtained with Hamiltonian (3) with no fitting parameters. The presence of a nonzero longitudinal field is necessary for nonstoquasticity, as there exists a unitary transformation that can remove positive off-diagonal elements at $h_i = 0$ (see Appendix A 3). The experimental parameters in Fig. 3(a) are the same as those in Fig. 2(b), except for the flux bias $\Phi_{q,i}^x$ determining h_i. This nonzero bias manifests itself in Fig. 3(a) as an avoided level crossing between the second and third excited states. Figure 3(b) shows the energy as a function of $\Phi_{q,1}^x$ when $\Phi_{q,2}^x = 0.1\ \mathrm{m}\Phi_0$ and $M_{12} = 0.55$ pH. The top-two energy levels cross when $\Phi_{q,1}^x = -\Phi_{q,2}^x$. The energy as a function of M_{12} is presented in Fig. 3(c). As in Fig. 3(a), the avoided level crossing observed at $M_{12} = 0.55$ pH is a result of nonzero energy bias ($h_i \approx 0.15$ GHz at this point). Zero-bias simulations are shown by the dashed lines. One can clearly see that the capacitive coupling introduces an asymmetry between the antiferromagnetic and ferromagnetic sides of the magnetic coupling. Without the coupling capacitor, the energy spectrum is expected to be symmetric about $M_{12} = 0$. The theoretical (solid) lines in Fig. 3(c) are produced with the reduced Hamiltonian (3) with the coupling parameters shown in Fig. 3(d). In Figs. 3(a)–3(c), theory agrees well with experiment, with no additional fitting.

B. Coherent oscillations

Finally, we measure quantum coherent oscillations in the coupled two-qubit system. Qubits are initialized in a computational-basis state by applying a strong flux bias $\Phi_{q,i}^x$. The coherent oscillations are induced by quickly (within 200 ps) pulsing down the barriers of both qubits simultaneously. Before we lower the barriers, the flux bias

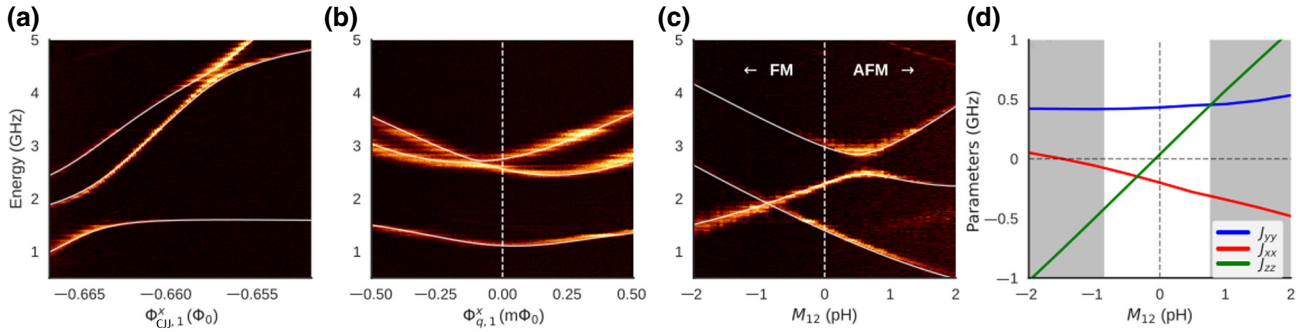

FIG. 3. Two-qubit spectra at nonzero energy bias $h_i \neq 0$. In all cases, qubit 2 is biased away from degeneracy with $\Phi_{q,2}^x = 0.1\ \mathrm{m}\Phi_0$ and $\Phi_{\mathrm{CJJ},2}^x$ is set such that the effective single-qubit tunneling $\Delta_2 = 1.5$ GHz. Energy is measured relative to the ground state. Solid white lines correspond to numerical simulations obtained with the two-qubit Hamiltonian (3) with no fitting parameters. (a) Energy as a function of $\Phi_{\mathrm{CJJ},1}^x$ at fixed $\Phi_{q,i}^x = 0.1\ \mathrm{m}\Phi_0$ and $M_{12} = 0$. (b) Energy as a function of $\Phi_{q,1}^x$ at $M_{12} = 0.55$ pH and effective single-qubit $\Delta_1 = 1.5$ GHz. The vertical dotted line goes through $\Phi_{q,1}^x = 0$ to highlight the asymmetry in the spectrum due to fixed $\Phi_{q,2}^x = 0.1\ \mathrm{m}\Phi_0$. (c) Energy as a function of M_{12} at $\Phi_{q,i}^x = 0.1\ \mathrm{m}\Phi_0$ and $\Delta_i = 1.5$ GHz. The dashed lines correspond to numerical simulations at zero energy biases. The observed avoided crossing at $M_{12} = 0.55$ pH is due to nonzero biases. The vertical dotted line separates ferromagnetic (FM) and antiferromagnetic (AFM) regions. The asymmetry in the data with respect to this line is due to capacitive coupling. (d) Extracted interaction parameters in Hamiltonian (3) that provide the theoretical (solid) lines in (c). The Hamiltonian is nonstoquastic in the white unshaded area according to Ref. [13].

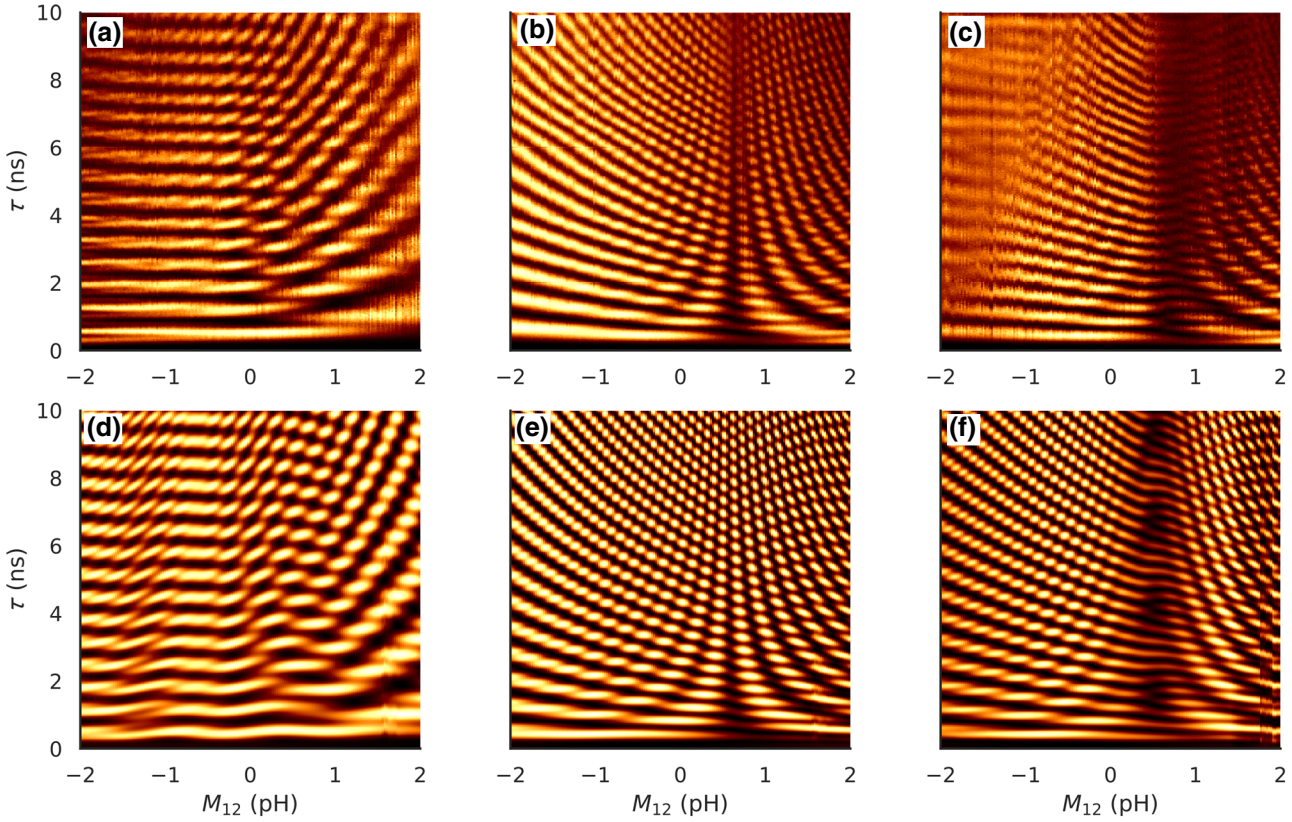

FIG. 4. Two-qubit coherent oscillations as a function of mutual inductance. (a) Population of state $|\downarrow\uparrow\rangle$ when the system is initialized in $|\uparrow\downarrow\rangle$. (b),(c) Population of state $|\downarrow\downarrow\rangle$ when the system is initialized in $|\uparrow\uparrow\rangle$. The final flux bias on qubits for (c) is set to 0.1 mΦ_0, corresponding to Figs. 3(c) and 3(d). For (a),(b) the final flux bias is zero. (d)–(f) Numerical simulations corresponding to (a)–(c), obtained with the reduced four-level model given in Eq. (3), respectively.

$\Phi^x_{q,i}$ on each qubit is changed from its value at the preparation pulse to its final value. Since the computational-basis states are not the eigenstates of the total Hamiltonian, the system undergoes coherent oscillations between these states. After some dwell time τ, the qubits are simultaneously quenched by rapidly raising their energy barriers via $\Phi^x_{\mathrm{CJJ},i}$, followed by qubit-state readout. We repeat this process for a range of dwell times τ and coupling strengths M_{12}.

In Figs. 4(a) and 4(b), we show the measured state population $P_{\uparrow\downarrow}$ and $P_{\downarrow\downarrow}$ for qubits initially prepared in $|\downarrow\uparrow\rangle$ and $|\uparrow\uparrow\rangle$ configurations, respectively, for $h_i = 0$. The agreement between time-domain experiments and numerical simulations, shown in Figs. 4(d) and 4(e), justifies the two-qubit Hamiltonian (3) as a valid description of the circuit in Fig. 1(a). Deviation between theory and experiment can be attributed to decoherence, which is absent in simulations. Single-qubit measurements reveal relaxation and dephasing times of $T_1 = 17$ ns and $T_2 = 16$ ns, respectively. These timescales are consistent with measurements of isolated flux qubits manufactured in the same stack but without the capacitive coupling.

Features of the energy as a function of M_{12} [Fig. 3(c)] are reflected in coherent oscillations [Figs. 4(c) and 4(f)]. The initial configuration, $|\uparrow\uparrow\rangle$, has significant overlap with the second and third excited states in the antiferromagnetic region ($M_{12} > 0$). The low oscillation frequency in the right half of Figs. 4(c) and 4(f) is therefore related to the gap between these two states. The minimum gap at $M_{12} \approx 0.55$ pH in Fig. 3(c) corresponds to the maximum slowdown at the same point in Figs. 4(c) and 4(f). When $h_1 = h_2 = 0$, this gap vanishes [see the dashed lines in Fig. 3(c)], nullifying the oscillations as seen in Figs. 4(b) and 4(e). This is a result of the destructive interference between the two-qubit cotunneling channels due to $\sigma^x_1\sigma^x_2$ and $\sigma^y_1\sigma^y_2$ terms and the indirect tunneling channels through sequential single-qubit flips caused by σ^x_1 and σ^x_2 terms in Hamiltonian (3), as schematically illustrated in Fig. 1(b). Moreover, we see an additional signature of J_{yy}, since without such coupling Fig. 4(a) would be a reflection of Fig. 4(b) with respect to $M_{12} = 0$ (see Appendix D).

IV. STOQUASTICITY

While the existence of J_{xx} or J_{yy} coupling is a necessary condition for nonstoquasticity, it is not sufficient. One needs to show that the sign problem survives all local transformations. While this is intractable at large scales

[12], it is feasible for two qubits [13]. To demonstrate this, we extract coefficients in Hamiltonian (3), which describes Fig. 3(c). Figure 3(d) plots interaction parameters except for J_{xz} and J_{zx}, which are negligibly small. Other parameters are provided in Appendix A 2. We see that the electrostatic coupling between the rf SQUIDs gives rise to a pronounced J_{yy} that is almost constant over the whole range of M_{12}. The two-qubit cotunneling mediated by the higher-energy states of the rf SQUIDs leads to a $\sigma_1^x\sigma_2^x$ coupling with coefficient J_{xx}. Both J_{xx} and J_{zz} depend on M_{12} and therefore cannot be tuned independently. The magnitude of J_{xx} is comparable to that of J_{yy} for large antiferromagnetic coupling. For rotations in the x-z plane, the J_{xx} and J_{zz} terms can both reduce the nonstoquastic contribution of J_{yy}. The Hamiltonian becomes stoquastic if either of them exceeds J_{yy} in magnitude, as highlighted by the shaded area in the Fig. 3(d). Applying all possible local unitary transformations outlined in Ref. [13], we confirm nonstoquasticity in the unshaded region. Note that Δ, J_{xx}, and J_{yy} depend on the barrier heights, with Δ and J_{yy} being proportional to each other (see Appendix A 3). As a result, the width of the nonstoquastic region changes with $\Phi^x_{\mathrm{CJJ},i}$, which controls the qubit tunneling amplitudes Δ.

V. CONCLUSION

In summary, we fabricate two superconducting flux qubits coupled both inductively and capacitively. Starting from a rf-SQUID model, with experimentally extracted circuit parameters, we obtain a reduced two-qubit Hamiltonian with $\sigma_1^x\sigma_2^x$, $\sigma_1^y\sigma_2^y$, and $\sigma_1^z\sigma_2^z$ interactions. We show that the reduced Hamiltonian can explain the findings of spectroscopy and the coherent-oscillation experiments. Considering all local transformations, we prove that the Hamiltonian is nonstoquastic over a wide range of parameters. Equilibrium statistics of such nonstoquastic quantum processors cannot be simulated by QMC methods due to the sign problem. Implementation of couplings via conjugate degrees of freedom such as charge and flux is an important step toward the development of universal quantum annealers [21–23]. Our implementation is based on current, scalable superconducting fabrication technology that is ready to be expanded to a large number of qubits. Finally, for large-scale systems, having $\sigma_i^y\sigma_j^y$ terms can make QMC simulation intractable even if the Hamiltonian is stoquastic. This is because finding a local transformation to cure the sign problem at large scale is by itself intractable [12].

ACKNOWLEDGMENTS

We are grateful to D. Lidar and M. Marvian for pointing out unitary transformations that cure the sign problem at zero bias. We also thank J. Biamonte, D. DiVincenzo, I. Hen, J. Klassen, P. Love, J. Raymond, P. Saint-Jean, and B. Terhal for fruitful discussions, and F. Hanington and A. King for carefully reading the manuscript.

APPENDIX A: SYSTEM HAMILTONIAN

Our goal here is to derive a Hamiltonian of two rf SQUIDs that have both, inductive and capacitive, couplings.

1. rf SQUID with a compound Josephson-junction loop

We begin with a description of a single rf SQUID having a symmetric compound Josephson-junction (CJJ) loop, as outlined in detail in Ref. [9] (see Fig. 1). The Hamiltonian of this system has three components:

$$H = H_q + H_{\mathrm{CJJ}} - E_J \cos\left(\frac{\pi\Phi_{\mathrm{CJJ}}}{\Phi_0}\right)\cos\left(2\pi\frac{\Phi_q}{\Phi_0}\right). \tag{A1}$$

Here the Hamiltonians H_q and H_{CJJ} describe the main body of the qubit and the CJJ loop, respectively. They are expressed as

$$H_\kappa = \frac{Q_\kappa^2}{2C_\kappa} + \frac{(\Phi_\kappa - \Phi_\kappa^x)^2}{2L_\kappa}, \quad \kappa = \{q, \mathrm{CJJ}\}. \tag{A2}$$

The third term in Eq. (A1) introduces an interaction between these two loops. The fluxes in the main body of the qubit and in the CJJ loop are denoted as Φ_q and Φ_{CJJ}, and their inductances are L_q and L_{CJJ}, respectively. The external fluxes applied to the main body of the qubit and to the CJJ loop are Φ_q^x and Φ_{CJJ}^x. The CJJ loop has two symmetric branches a and b. Each of them has one Josephson junction, with capacitance C_a (C_b) and with a persistent current I_a (I_b). The total current flowing through both branches of the CJJ loop is denoted as $I_c = I_a + I_b$, with the total Josephson energy $E_J = \Phi_0 I_c/2\pi$, where $\Phi_0 = \pi\hbar/e$ is the flux quantum, where e is the electron charge. The effective capacitances of the main qubit and the CJJ loop are $C_q = C_a + C_b$ and $C_{\mathrm{CJJ}} = C_aC_b/(C_a + C_b)$, respectively. The charge, $Q_\kappa = -i\hbar(\partial/\partial\Phi_\kappa)$, and flux, Φ_κ, are conjugate operators obeying the commutator $[\Phi_\kappa, Q_\kappa]_- = i\hbar$.

For qubits 1 and 2 studied in the main text we have $L_{\mathrm{CJJ},1} = 17.0$ pH and $L_{\mathrm{CJJ},2} = 17.2$ pH, while the body inductances are $L_1 = 231.9$ pH and $L_2 = 239.0$ pH. When $L_{\mathrm{CJJ}} \ll L_q$, the dynamics of the fast degrees of freedom described by the operator Φ_{CJJ} is determined by the ground state of the Hamiltonian H_{CJJ} (see Ref. [9]). This ground-state adiabatically follows the flux degrees of freedom, Φ_q, in the main body of the rf SQUID. One can then ignore the kinetic part of the Hamiltonian H_{CJJ} and define an effective potential of the main loop by finding the minimum

potential energy of the system (A1) for each given flux Φ_q:

$$U_{\text{eff}}(\Phi_q) = \min_{\Phi_{\text{CJJ}}} U(\Phi_q, \Phi_{\text{CJJ}}), \tag{A3}$$

where

$$U(\Phi_q, \Phi_{\text{CJJ}}) = \sum_{\kappa=q,\text{CJJ}} \frac{(\Phi_\kappa - \Phi_\kappa^x)^2}{2L_\kappa} - E_J \cos\left(\frac{\pi\Phi_{\text{CJJ}}}{\Phi_0}\right) \cos\left(2\pi\frac{\Phi_q}{\Phi_0}\right). \tag{A4}$$

This leads to the following effective Hamiltonian for the rf SQUID:

$$H = \frac{Q_q^2}{2C_q} + U_{\text{eff}}(\Phi_q). \tag{A5}$$

As a rough approximation, the effective potential energy of the rf SQUID can be written as

$$U_{\text{eff}}(\Phi_q) = \frac{(\Phi_q - \Phi_q^x)^2}{2L_q} - E_J(\Phi_{\text{CJJ}}^x) \cos\left(2\pi\frac{\Phi_q}{\Phi_0}\right), \tag{A6}$$

with a tunable Josephson energy

$$E_J(\Phi_{\text{CJJ}}^x) = \frac{\Phi_0 I_c}{2\pi} \cos\left(\pi\frac{\Phi_{\text{CJJ}}^x}{\Phi_0}\right). \tag{A7}$$

However, in our simulations, we do not use the above approximation but actually do the minimization with respect to Φ_{CJJ} as given in Eq. (A3) and described in detail in Ref. [9].

We now analyze two rf SQUIDs connected by a mutual inductance M_{12} and by a capacitor C_{12} as depicted in Fig. 1(a). The inductive coupling between the main loops of the SQUIDs is given by the formula

$$U_M = \frac{M_{12}}{L_1 L_2}(\Phi_{q,1} - \Phi_{q,1}^x)(\Phi_{q,2} - \Phi_{q,2}^x), \tag{A8}$$

where $L_i \equiv L_{qi}$ $(i = 1, 2)$.

The kinetic energy of two electrostatically coupled SQUIDs, with capacitances $C_i \equiv C_{qi}$, has the form

$$K = \sum_i \frac{C_i \dot{\Phi}_{q,i}^2}{2} + \frac{C_{12}(\dot{\Phi}_{q,2} - \dot{\Phi}_{q,1})^2}{2}, \tag{A9}$$

where we use the relation $V_i = \dot{\Phi}_{q,i}$ between a voltage V_i on the ith junction and the flux $\Phi_{q,i}$. Charge $Q_i = \partial\mathcal{L}/\partial\dot{\Phi}_{q,i}$ of the ith qubit is defined as a derivative of the two-qubit Lagrangian

$$\mathcal{L} = K - \sum_{i=1}^{2} U_{\text{eff},i}(\Phi_{q,i}) - U_{12}, \tag{A10}$$

where $U_{\text{eff},i}(\Phi_{q,i})$ is the effective potential energy of the i qubit [see Eqs. (A3) and (A6)]. Using Eqs. (A9) and (A10), we obtain the relation between charge and time derivatives of flux:

$$\begin{aligned} Q_1 &= (C_1 + C_{12})\dot{\Phi}_{q,1} - C_{12}\dot{\Phi}_{q,2}, \\ Q_2 &= (C_2 + C_{12})\dot{\Phi}_{q,2} - C_{12}\dot{\Phi}_{q,1}. \end{aligned} \tag{A11}$$

We can now write the total Hamiltonian of two coupled rf SQUIDs, $H = \sum_i \dot{\Phi}_{q,i} Q_i - \mathcal{L}$, as

$$H = \sum_{i=1}^{2} H_i + U_M + U_C. \tag{A12}$$

Here

$$H_i = \frac{Q_i^2}{2\tilde{C}_i} + U_{\text{eff},i}(\Phi_{q,i}) \tag{A13}$$

is the Hamiltonian of the i qubit. The qubits are now characterized by the loaded capacitances:

$$\begin{aligned} \tilde{C}_1 &= C_1 + \frac{C_{12}C_2}{C_2 + C_{12}}, \\ \tilde{C}_2 &= C_2 + \frac{C_{12}C_1}{C_1 + C_{12}}. \end{aligned} \tag{A14}$$

The inductive interaction between qubits is given by (A8). The capacitive coupling is determined by the potential

$$U_C = \frac{C_{12}\, Q_1 Q_2}{C_1 C_2 + (C_1 + C_2)C_{12}}. \tag{A15}$$

At large scales, the capacitative network renormalizes the capacitances of each rf SQUID. In addition, capacitative loading should reduce the sensitivity of the qubits to charge fluctuations, thus making this device more immune to charge noise.

2. Reduction approach

Diagonalizing the single-SQUID Hamiltonian H_i (A13), we obtain a set of energy eigenstates, $|\chi_\mu^i\rangle$, and eigenenergies, ε_μ^i, such that

$$H_i = \sum_{\mu=1}^{N_i} \varepsilon_\mu^i \, |\chi_\mu^i\rangle \langle\chi_\mu^i| \,. \tag{A16}$$

For each SQUID we take into account a large number, $N_i \gg 1$, of the energy eigenstates and write the Hamiltonian (A12) of two coupled rf SQUIDs in the basis formed

by direct products $|\chi_\mu^1 \otimes \chi_\nu^2\rangle \equiv |\chi_\mu^1\rangle \otimes |\chi_\nu^2\rangle$:

$$H = \sum_{\mu=1}^{N_1} \varepsilon_\mu^1 \, |\chi_\mu^1\rangle \, \langle\chi_\mu^1| + \sum_{\nu=1}^{N_2} \varepsilon_\nu^2 \, |\chi_\nu^2\rangle \, \langle\chi_\mu^2| + U_M + U_C. \tag{A17}$$

Here charge and flux operators should be also written in the $|\chi_\mu^1 \otimes \chi_\nu^2\rangle$ basis. The eigenstates, $|\eta_a\rangle$, of the Hamiltonian (A17) become

$$|\eta_a\rangle = \sum_{\mu}^{N_1} \sum_{\nu}^{N_2} c_{\mu\nu}^a \, |\chi_\mu^1 \otimes \chi_\nu^2\rangle \, , \tag{A18}$$

where the amplitudes are given as

$$c_{\mu\nu}^a = \langle \chi_\mu^1 \otimes \chi_\nu^2 | \eta_a \rangle. \tag{A19}$$

The two-SQUID Hamiltonian,

$$H = \sum_{a=1}^{N} \varepsilon_a \, |\eta_a\rangle \, \langle\eta_a| \, , \tag{A20}$$

is characterized by the energy spectrum ε_a, with a total number of levels $N = N_1 N_2$.

Working with continuous models becomes computationally challenging beyond a small number of coupled rf SQUIDs. With the goal to use rf SQUIDs as qubits, one needs to reduce the continuous Hamiltonian to a discrete (qubit) Hamiltonian. For uncoupled SQUIDs, we choose the following superpositions of the two lowest-energy states with the mixing angle θ_i:

$$\begin{aligned} |\downarrow\rangle_i &= \cos\theta_i \, |\chi_1^i\rangle + \sin\theta_i \, |\chi_2^i\rangle \\ |\uparrow\rangle_i &= -\sin\theta_i \, |\chi_1^i\rangle + \cos\theta_i \, |\chi_2^i\rangle \, . \end{aligned} \tag{A21}$$

The basis states $|\downarrow_i\rangle$ and $|\uparrow_i\rangle$ correspond to the left and right circulating currents, or, equivalently, to the left and right sides of the SQUID potential well. The mixing angle θ_i is chosen to maximize the left-well population in the state $|\downarrow_i\rangle$ and thus the right-well population when the SQUID is in the state $|\uparrow_i\rangle$. The interaction Hamiltonian mixes the states $|\downarrow_i\rangle \, , |\uparrow_i\rangle$ with higher-energy states of the individual rf SQUIDs that one needs to take into account for a correct description of the coupled system.

Since we are interested in the low-energy spectrum of the coupled system, the number of eigenstates taken into account in Eqs. (A16) and (A17) can be truncated to just two states for each rf SQUID. With this truncation, four eigenvectors, $|\eta_a\rangle$ $(a = 1, \ldots, 4)$, of the two-SQUID system are approximated as

$$|\eta_a\rangle \simeq \frac{1}{N_a} \sum_{\mu=1}^{2} \sum_{\nu=1}^{2} c_{\mu\nu}^a \, |\chi_\mu^1 \otimes \chi_\nu^2\rangle \, , \tag{A22}$$

where the amplitudes $c_{\mu\nu}^a$ are given in Eq. (A19), and the normalization coefficient is calculated as

$$N_a = \sqrt{\sum_{\mu=1}^{2} \sum_{\nu=1}^{2} |c_{\mu\nu}^a|^2}.$$

We apply the Gram-Schmidt procedure to the four states given in Eq. (A22) to obtain the orthonormalized set of the two-qubit basis states obeying the relation $\langle\eta_a|\eta_b\rangle = \delta_{ab}$. This reduction approach works only in the limit where $N_a \approx 1$ for $a = 1, \ldots, 4$. In this case most of the population of the two-SQUID system is distributed over the tensor products $|\chi_\mu^1 \otimes \chi_\nu^2\rangle$ of the two lowest eigenstates of the isolated rf SQUIDs $(\mu, \nu = 1, 2)$.

To derive the reduced Hamiltonian of two coupled SQUIDs we start with a Hamiltonian (A20) truncated to the four lowest-energy states. In the energy basis this Hamiltonian is described by the diagonal matrix: $H = \mathrm{diag}(\varepsilon_1, \varepsilon_2, \varepsilon_3, \varepsilon_4)$. The Hamiltonian H can be written in the χ basis formed by the four vectors $|\chi_\mu^1 \otimes \chi_\nu^2\rangle$ $(\mu, \nu = 1, 2)$ by applying the rotation matrix $R_1 = (|\eta_1\rangle \; |\eta_2\rangle \; |\eta_3\rangle \; |\eta_4\rangle)$ such that $H_\chi = R_1 H R_1^T$. Finally, the unitary matrix $R_2 = (|1\rangle \; |2\rangle \; |3\rangle \; |4\rangle)$ rotates the Hamiltonian into the computational basis, formed by the vectors:

$$\begin{aligned} |1\rangle &= |\downarrow_1 \otimes \downarrow_2\rangle \, , \; |2\rangle = |\downarrow_1 \otimes \uparrow_2\rangle \, , \\ |3\rangle &= |\uparrow_1 \otimes \downarrow_2\rangle \, , \; |4\rangle = |\uparrow_1 \otimes \uparrow_2\rangle \, . \end{aligned} \tag{A23}$$

After this rotation the Hamiltonian $H = R_2 H_\chi R_2^T$ can be represented by the 4×4 matrix,

$$H = \begin{pmatrix} J_{zz} - h_1 - h_2 & -\Delta_2/2 & -\Delta_1/2 & J_{xx} - J_{yy} \\ -\Delta_2/2 & -J_{zz} - h_1 + h_2 & J_{xx} + J_{yy} & -\Delta_1/2 \\ -\Delta_1/2 & J_{xx} + J_{yy} & -J_{zz} + h_1 - h_2 & -\Delta_2/2 \\ J_{xx} - J_{yy} & -\Delta_1/2 & -\Delta_2/2 & J_{zz} + h_1 + h_2 \end{pmatrix}, \tag{A24}$$

or by the Hamiltonian of two coupled spins (qubits):

$$H = -\frac{\Delta_1}{2}\sigma_1^x - \frac{\Delta_2}{2}\sigma_2^x + h_1\sigma_1^z + h_2\sigma_2^z + \sum_{\alpha,\beta} J_{\alpha\beta}\sigma_1^\alpha\sigma_2^\beta, \tag{A25}$$

where $\alpha, \beta = x, y, z$. We use the following representation of the Pauli matrices:

$$\begin{aligned} \sigma_i^x &= |{\downarrow_i}\rangle\langle{\uparrow_i}| + |{\uparrow_i}\rangle\langle{\downarrow_i}|, \\ \sigma_i^y &= i(|{\downarrow_i}\rangle\langle{\uparrow_i}| - |{\uparrow_i}\rangle\langle{\downarrow_i}|), \\ \sigma_i^z &= |{\uparrow_i}\rangle\langle{\uparrow_i}| - |{\downarrow_i}\rangle\langle{\downarrow_i}|. \end{aligned} \tag{A26}$$

The parameters of the Hamiltonian (A25) are extracted by comparing the operator $H = R_2 H_\chi R_2^T$ with the matrix (A24). Note that $J_{yx} = J_{xy} = J_{yz} = J_{zy} = 0$, since the Hamiltonian is real and the coefficients J_{xz} and J_{zx} are negligible: $J_{xz}, J_{zx} \ll \Delta_1, \Delta_2$. The non-negligible parameters of the Hamiltonian H describing interactions between the qubits are shown in Fig. 3(d).

Figure 5(a) shows how the Hamiltonian parameters change during the annealing, which is performed by changing $\Phi^x_{\mathrm{CJJ},i}$. All off-diagonal terms vanish as $\Phi^x_{\mathrm{CJJ},i}$ varies from right to left as the annealing proceeds. Linear dependence of J_{xx} and J_{yy} on Δ_i is evident from Fig. 5(b).

One can equivalently use the projection technique in Ref. [37] to derive a reduced Hamiltonian for two interacting subsystems, namely, our SQUIDs. The reduced Hamiltonian obtained with the projection approach agrees with the two-qubit Hamiltonian given by Eqs. (A24) and (A25).

3. Unitary transformations and stoquasticity

Hamiltonian (A24) can have positive off-diagonal matrix elements under several conditions but not all of those make the Hamiltonian nonstoquastic. One has to take into account all local transformations of the basis before deciding about nonstoquasticity of the Hamiltonian. Using the unitary transformation $H \to U^\dagger H U$, with $U = \otimes_i (\sigma_i^z)^{(1-\mathrm{sign}\,\Delta_i)/2}$, one can make all $\Delta_i\sigma_i^x$ terms in the Hamiltonian nonpositive regardless of the sign of Δ_i. Hamiltonian (A24) has positive matrix elements if $|J_{yy}| > |J_{xx}|$, since matrix elements H_{14} and H_{23} have opposite signs, due to J_{yy}, making one of them positive. However, this condition is not sufficient for nonstoquasticity. To demonstrate this fact, we apply a Hadamard rotation on both qubits turning the x axis to the z axis and vice versa, so that $\sigma_i^x = \tau_i^z$, $\sigma_i^y = \tau_i^y$, and $\sigma_i^z = -\tau_i^x$. Here τ_i^x, τ_i^y, and τ_i^z are Pauli matrices of the i qubit in the rotated frame. After the Hadamard rotation the two-qubit Hamiltonian has the form

$$H = \begin{pmatrix} J_{xx} + \Delta_1/2 + \Delta_2/2 & -h_2 & -h_1 & J_{zz} - J_{yy} \\ -h_2 & -J_{xx} + \Delta_1/2 - \Delta_2/2 & J_{zz} + J_{yy} & -h_1 \\ -h_1 & J_{zz} + J_{yy} & -J_{xx} - \Delta_1/2 + \Delta_2/2 & -h_2 \\ J_{zz} - J_{yy} & -h_1 & -h_2 & J_{xx} - \Delta_1/2 - \Delta_2/2 \end{pmatrix}. \tag{A27}$$

This Hamiltonian has positive matrix elements at $|J_{yy}| > |J_{zz}|$. At nonzero biases, $h_i \neq 0$ (and at non-zero Δ_i), only rotations in the x-z plane are allowed [13] since rotations in the x-y and z-y planes introduce complex matrix elements in the Hamiltonian. In Fig. 3(d), we search over all possible local rotations outlined in detail in Ref. [13] and

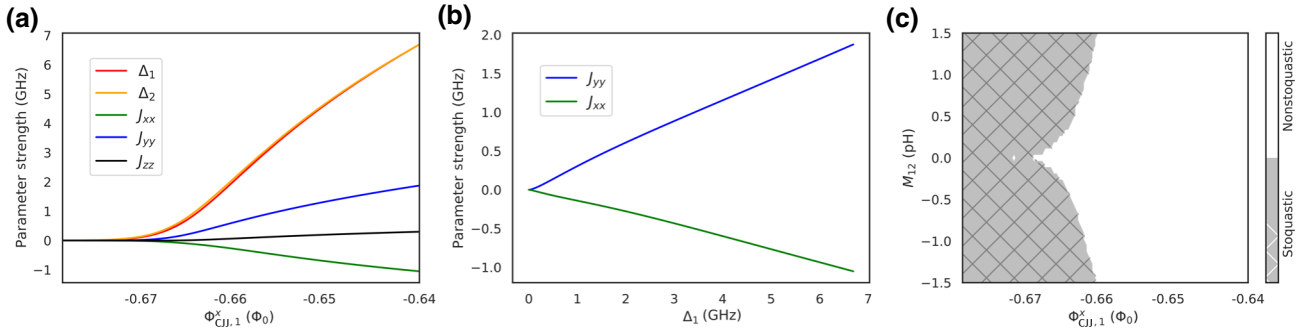

FIG. 5. (a) Two-qubit-Hamiltonian parameters as functions of $\Phi^x_{\mathrm{CJJ},i}$, which controls the barrier height, at zero flux bias and zero inductive coupling. (b) J_{xx} and J_{yy} as a function of Δ_i for the same setting as in (a). (c) The nonstoquastic region as a function of mutual inductance and $\Phi^x_{\mathrm{CJJ},i}$ for nonzero flux bias. The Hamiltonian is nonstoquastic in the white area.

find, in particular, that at the borders of the nonstoquastic range the $\sigma^z\sigma^z$ coupling is on order of the $\sigma^y\sigma^y$ interaction strength: $|J_{zz}| \sim |J_{yy}|$. Figure 5(c) is an extension of this figure, displaying the nonstoquastic region as a function of M_{12} and $\Phi^x_{\mathrm{CJJ},i}$, which varies during annealing. It follows from Figs. 5(a) and 5(c) that during the critical region of annealing, when off-diagonal elements of the Hamiltonian are present, the Hamiltonian can be nonstoquastic depending on the magnitude of the coupling.

The matrix (A27) also provides the intuition necessary to see the effects of the J_{xx}, h_1, and h_2 terms on experimentally measured spectra. When $J_{zz} = 0$ and $h_1 = h_2 = 0$, the Hamiltonian is block diagonal as there is no interaction between aligned and antialigned states. In the absence of the J_{xx} term, the eigenvalues of the Hamiltonian become $\pm\sqrt{J_{yy}^2 + [(\Delta_1 \pm \Delta_2)/2]^2}$. Without the J_{xx} term, the two highest eigenvalues can cross only if $\Delta_1\Delta_2 = 0$. However we see a clear level crossing in the energy-versus-$\Phi^x_{\mathrm{CJJ},1}$ plots in Figs. 9(d)–9(f), where $\Delta_i \neq 0$. This is a clear signature of a J_{xx}-type interaction. Furthermore, the second and third excited states, which cross in the presence of J_{xx}, belong to two separate blocks of the Hamiltonian. When $h_i \neq 0$, the Hamiltonian is no longer block diagonal and the two highest excited states start interacting. Hence, the avoided crossings visible in the energy-versus-$\Phi^x_{\mathrm{CJJ},1}$ and energy-versus-M_{12} plots in Figs. 3(a) and 3(c) are clear signatures of nonzero h_1 and h_2 .

APPENDIX B: QUBIT AND COUPLER PARAMETER CHARACTERIZATION

1. Coupler characterization

We follow Ref. [10] for the characterization of the tunable magnetic coupler. In Fig. 6, we show the measured coupler M_{12} versus the coupler flux bias Φ^x_{co}.

The data are fitted to a classical model:

$$M_{12} = \frac{M^2_{\mathrm{co},q}}{L_{\mathrm{co}}} \frac{\beta \cos\varphi^x_{\mathrm{co}}/2}{1 + \beta\cos\varphi^x_{\mathrm{co}}/2} + M^{(0)}_{12}, \qquad \text{(B1)}$$

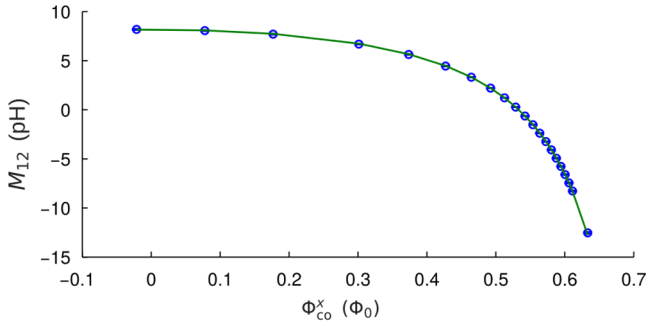

FIG. 6. Measured coupler M_{12} versus coupler flux bias Φ^x_{co} and a fit to the classical model of the coupler.

where $M_{\mathrm{co},q}$ is the mutual inductance between the qubit and the coupler, L_{co} is the coupler inductance, $\beta = 2\pi L_{\mathrm{co}} I_{c,\mathrm{co}}/\Phi_0$, $M^{(0)}_{12}$ is the stray mutual inductance between the qubits, and $\varphi^x_{\mathrm{co}} = 2\pi\Phi^x_{\mathrm{co}}$ is the normalized external bias of the coupler. From the fitting, we obtain $M^2_{\mathrm{co},q}/L_{\mathrm{co}} = 10.77$ pH, $\beta = 1.416$, and $M^{(0)}_{\mathrm{eff}} = 1.848$ pH. Using Eq. (B1) and the above fitting parameters, we can set the coupler to any coupling strength within the range $|M_{12}| \leq 8.145$ pH.

2. Quasistatic qubit characterization

When the tunneling barrier is high, where the single-qubit tunneling is largely suppressed, the properties of a flux qubit can be described by a classical model [9]. In this regime, we measure persistent current versus Φ^x_{CJJ} across a range of three flux quantum Φ_0. Fits to the classical model (see Fig. 7) yield the following qubit parameters: $I_{c,1} = 3.227$ μA, $I_{c,2} = 3.157$ μA, $L_1 = 231.6$ pH, and $L_2 = 239.0$ pH.

3. Single-qubit spectroscopy

The qubit energy eigenstates can be characterized by microwave spectroscopy. In Fig. 8(a), we show the pulse sequence for measuring the qubit spectra and the effective qubit potential at each segment of the pulse sequence. The qubit is first initialized in its ground state by adiabatically preparing a symmetric double-well potential with a relatively low tunneling barrier. In this limit, the qubit frequency, which is set by the tunneling amplitude, is much larger than 1 GHz ($\Delta \gg k_B T$). Then we apply a microwave pulse Φ^x_q to excite the qubit to its excited state. We sweep the frequency of the microwave pulse from 0.5 to 8 GHz to probe all excited states in that range. After the microwave pulse, an adiabatic tilt followed by a quench, which increases the barrier height, is applied to the qubit to project the qubit ground and excited states to the clockwise and counterclockwise persistent-current states for readout. The same pulse sequence was used in Ref. [35]. In this

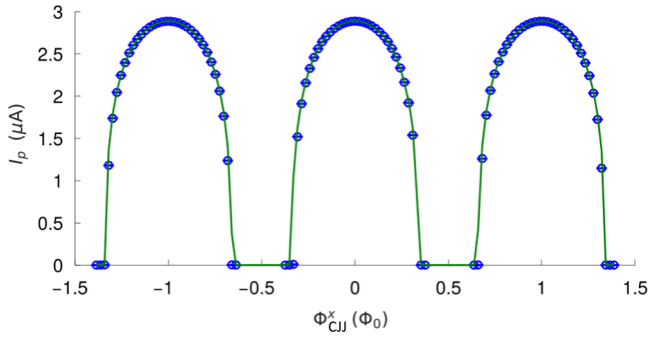

FIG. 7. Measured persistent current I_p versus Φ^x_{CJJ}, which controls the barrier height of the double-well potential, and a fit to the classical model of qubit 1.

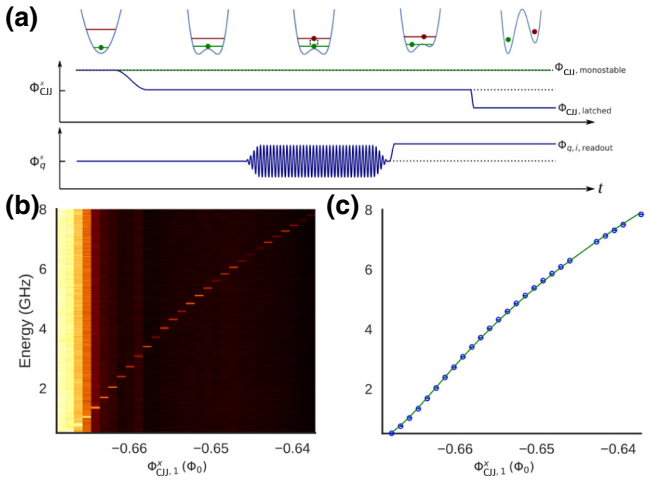

FIG. 8. (a) Pulse sequence and the effective qubit potential at each pulse segment for the single-qubit-spectroscopy experiments. (b) Color plot of the microwave-spectroscopy data versus the flux bias $\Phi^x_{\rm CJJ}$, which controls the barrier height for qubit 1. (c) Extracted spectroscopy peak positions that represent the qubit frequency versus $\Phi^x_{\rm CJJ}$ and a fit to the numerical rf-SQUID model.

experiment, we use a rise time of 1 ns for both the adiabatic tilt and the quench on the barrier height. Throughout the single-qubit-spectroscopy experiments, we keep the magnetic coupling strength at $M_{12} = 0$ and the other qubit at $\Phi^x_{\rm CJJ} = 0.5\Phi_0$. In Fig. 8(b), we show the energy versus $\Phi^x_{\rm CJJ,1}$ for qubit 1. The extracted qubit frequency from Fig. 8(b) and the fit to the rf-SQUID numerical model are shown in Fig. 8(c).

Effective single-qubit Δ corresponds to the energy gap between the ground state and the first excited state in the single-qubit-spectroscopy measurements. Once we have an accurate model that predicts the location of the first excited state, the appropriate $\Phi^x_{{\rm CJJ},i}$ that needs to be applied to set the qubit to a given Δ is determined with the model extracted above. Note that the effective single-qubit Δ is influenced by the capacitive coupling that is always present. As a result, the individual qubit dynamics are always affected by the presence of the secondary qubit even if it is in a monostable state ($\Phi^x_{\rm CJJ} = 0.5\Phi_0$).

4. Two-qubit spectroscopy

The coupled-system energies can be probed by microwave spectroscopy in a way that is similar to single-qubit spectroscopy. In the main text we show the pulse sequence for the two-qubit spectroscopy. Although a microwave pulse is applied only to qubit 1, the energy eigenstates of both qubits are read out by simultaneous adiabatic tilts followed by a quench. Figure 8(b) shows spectroscopy data plotted as energy versus $\Phi^x_{\rm CJJ}$, which controls the barrier height of qubit 1. The barrier height of the second qubit is set to an effective single-qubit tunneling amplitude of Δ_2. Using the previously extracted circuit parameters and initializing the fitting procedure by the design values for the unknown parameters, we extract $C_1 = 119.5$ fF, $C_2 = 116.4$ fF, $C_{12} = 132.0$ fF, $L_{{\rm CJJ},1} = 17.016$ pH and $L_{{\rm CJJ},2} = 17.175$ pH. At this point, we have all the circuit parameters of this system as summarized in Table I.

We also perform similar two-qubit spectroscopy for various Δ_2 and M_{12} at $h_1 = h_2 = 0$ and compare the system energy spectra with numerical simulations using previously extracted parameters. In Fig. 9, we show the two-qubit-spectroscopy data and calculated energy spectra of the system for all combinations of $\Delta_2/h = 1.5$, 2.0, and 3.0 GHz and $M_{12} = 0$ and ± 2 pH. Very good agreement between the numerical model and the data is achieved. In all figures the solid (dashed) lines represent excitations from the ground (first excited) state.

APPENDIX C: PULSE-DISTORTION COMPENSATION FOR COHERENT OSCILLATIONS

Distortion of a short-duration pulse (10 ns or less) imposes a great limitation on the fidelity of coherent qubit operation. In our experiment, the qubit control involves applying fast pulses to lower and raise the tunneling barrier of the flux qubits. These pulses have short rise and fall times (approximately 200 ps). Here we discuss our method of measuring and correcting pulse distortion *in situ*.

We first measure the single-qubit coherent oscillations at $\Delta/h = 5$ GHz, where the qubit population in the computational basis is supposed to oscillate at frequency Δ. Pulse distortion is caused mainly by reflections. As a result, the $\Phi^x_{\rm CJJ}(t)$ signal reaching the qubit deviates from the ideal square pulse, which may distort the frequency of the coherent oscillations from the target Δ at a given time τ. To measure the distorted pulse in the time domain, we slice the coherent-oscillation data into small time windows, typically with a length of 400 ps, that contain more than one period of oscillation. We then extract the

TABLE I. Extracted parameters for the circuit in Fig. 1(a).

Qubit	$I_{c,i}$ (μA)	L_i (pH)	$L_{{\rm CJJ},i}$ (pH)	C_i (fF)	C_{12} (fF)	$\lvert M_{12}\rvert$ (pH)
1	$3.22697 \pm 4.1 \times 10^{-5}$	$231.633 \pm 4.5 \times 10^{-3}$	$17.02 \pm 6 \times 10^{-2}$	119.5 ± 0.89	132.0 ± 1.54	≤ 8.145
2	$3.15711 \pm 3.6 \times 10^{-5}$	$238.981 \pm 4.1 \times 10^{-3}$	$17.17 \pm 7.9 \times 10^{-2}$	116.4 ± 1.04		

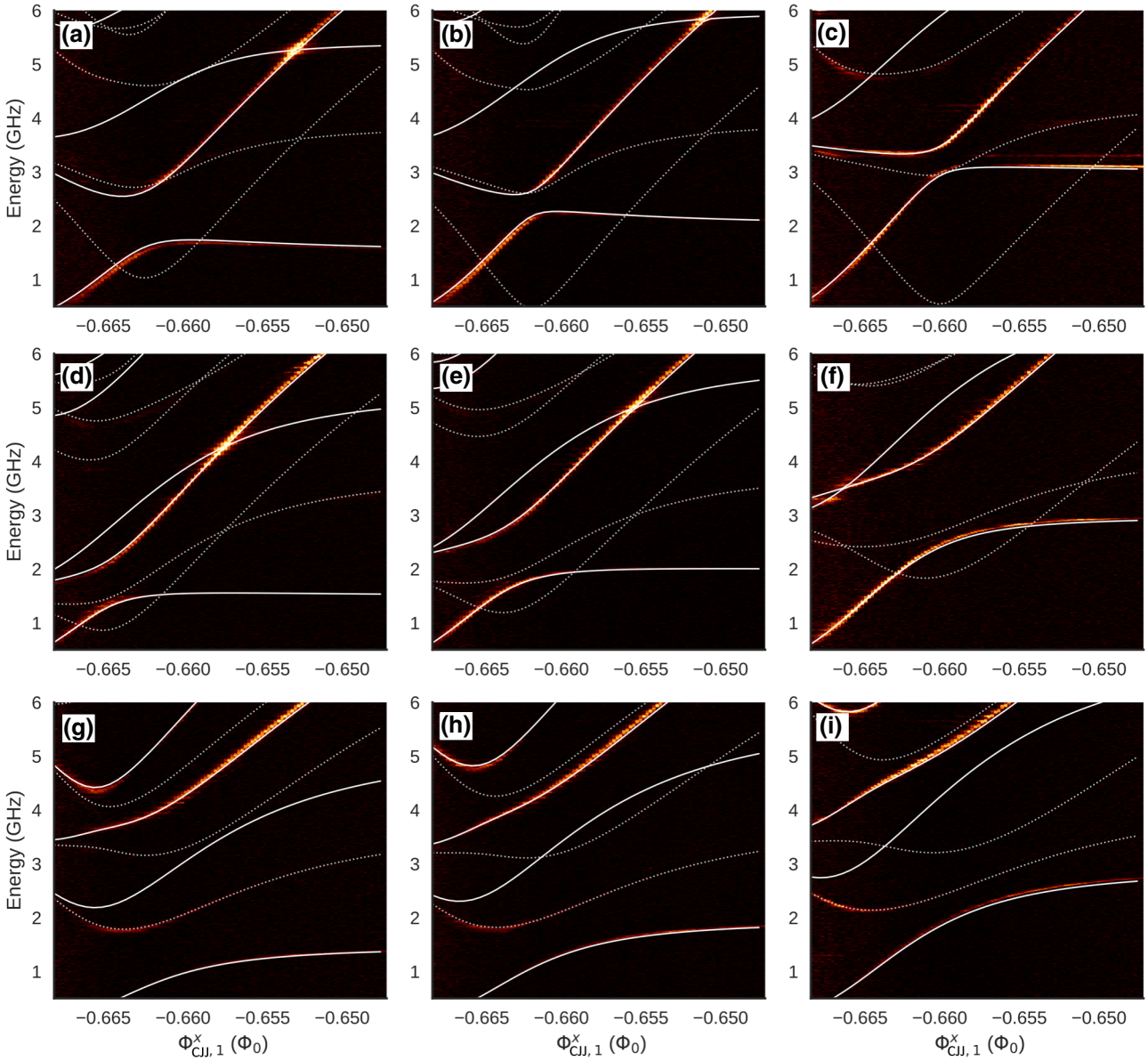

FIG. 9. Two-qubit-spectroscopy energy versus $\Phi^x_{CJJ,1}$ at (a) $\Delta_2/h \approx 1.5$ GHz and $M_{12} = -2.0$ pH, (b) $\Delta_2/h \approx 2.0$ GHz and $M_{12} = -2.0$ pH, (c) $\Delta_2/h \approx 3.0$ GHz and $M_{12} = -2.0$ pH, (d) $\Delta_2/h \approx 1.5$ GHz and $M_{12} = -0.0$ pH, (e) $\Delta_2/h \approx 2$ GHz and $M_{12} = 0.0$ pH, (f) $\Delta_2/h \approx 3.0$ GHz and $M_{12} = 0.0$ pH, (g) $\Delta_2/h \approx 1.5$ GHz and $M_{12} = 2.0$ pH, (h) $\Delta_2/h \approx 2.0$ GHz and $M_{12} = 2.0$ pH, and (i) $\Delta_2/h \approx 3.0$ GHz and $M_{12} = 2.0$ pH. The solid and dashed lines represent numerical calculations of energy differences. The solid lines correspond to excitations from the ground state and the dashed lines correspond to excitations from the first excited state.

coherent-oscillation frequency $\Omega(\tau)$ in each slice starting at time τ and treat this frequency as a measurement of the instantaneous $\Delta_m(\tau) = \Omega(\tau)$. The pulse distortion at any given time is then calculated by $\delta\Phi^x_{CJJ}(\tau) = [\Delta_m(\tau) - \Delta]/(\partial\Delta/\partial\Phi^x_{CJJ})$, where $\partial\Delta/\partial\Phi^x_{CJJ}$ can be evaluated numerically with the qubit model. To correct for the pulse distortion, we simply apply the first-order correction to the applied pulse with $\Phi^x_{CJJ,corr}(\tau) = \Phi^x_{CJJ}(\tau) + \delta\Phi^x_{CJJ}(\tau)$ at the same time τ. As the above correction at time τ may lead to distortions at times $t > \tau$, we iterate the entire measurement and correction procedure until the corrected pulse converges. In practice, this pulse-distortion correction procedure converges within five iterations. In Fig. 10, we show the coherent-oscillation data and the extracted instantaneous tunneling amplitude Δ_m with uncorrected (blue) and corrected (green) pulses Φ^x_{CJJ}. The measured tunneling amplitude Δ_m/h is fixed to the target value of 5 GHz after the pulse-distortion compensation is applied, which greatly increases the fidelity of the coherent oscillation.

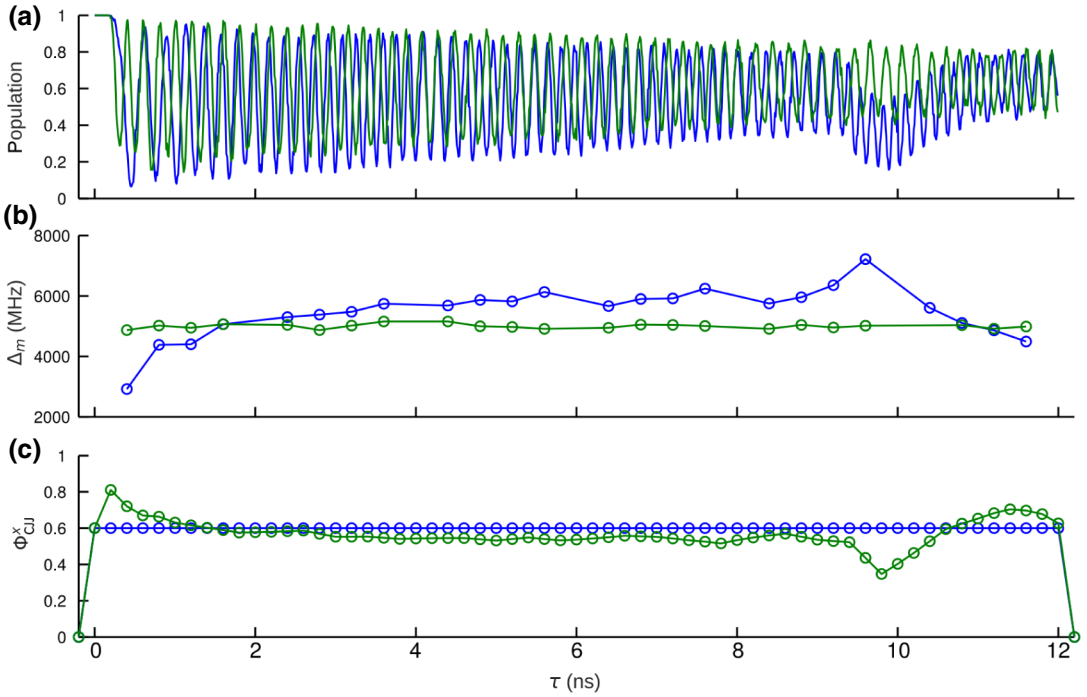

FIG. 10. Characterization and compensation of pulse distortion. (a) The coherent-oscillation data, (b) measured tunneling amplitude Δ_m, and (c) applied barrier pulses without (blue) and with (green) pulse-distortion corrections.

APPENDIX D: COHERENT-OSCILLATION PROTOCOL

The pulse sequence and the effective two-qubit potential at each pulse segment of a coherent-oscillation protocol are shown in Fig. 11. The qubits are initialized in two steps. A large flux bias, $\Phi^x_{q,\mathrm{prep}}$, is applied to tilt the potential in its monostable state. Next the tunneling strength is reduced, keeping the potential tilted. Once both qubits are prepared in a computational-basis state controlled by the signs of

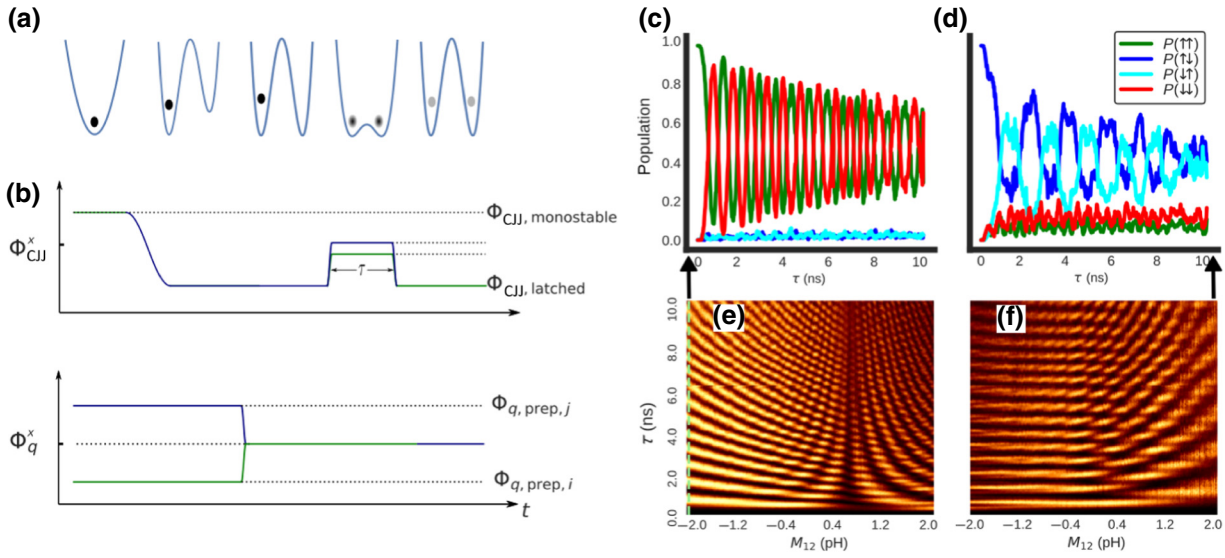

FIG. 11. (a) The effective qubit potential during each segment of the coherent-oscillation pulse shown in (b). The potential landscape represents a cut across the landscape depicted in Fig. 1(b). Its direction depends on the initial tilt pulse applied on the two qubits. Two-qubit coherent oscillation between the computational-basis states with strong (c) ferromagnetic coupling at $M_{12} = -2$ pH and strong (d) antiferromagnetic coupling at $M_{12} = 2$ pH versus time. Color plots of the two-qubit coherent oscillation versus the magnetic coupling strength M_{12} with the system initially prepared at (e) $|\downarrow\downarrow\rangle$ and (f) $|\downarrow\uparrow\rangle$.

$\Phi_{q,\mathrm{prep}}$ pulses, the tilts are removed. The coherent oscillations are induced by reducing the barriers of both qubits simultaneously to allow quantum fluctuations to drive the coherent dynamics of the system. As the computational-basis states are not the eigenstates of the total Hamiltonian, the system undergoes coherent oscillations between the computational-basis states with near-degenerate Ising energies. After some time τ, the states are read out by measuring qubit persistent currents after simultaneously quenching both qubits. The rise and fall times of the pulse, about 200 ps, are much faster than the dynamics of the qubits to snapshot the qubit population at the end of evolution. We repeat this process for a range of dwell times τ and magnetic coupling strengths. This protocol works equally well for a single-qubit if the qubit potential is kept in its monostable state.

In coherent-oscillation experiments, the system is prepared and measured in one of the four computational-basis states $|\uparrow\uparrow\rangle$, $|\uparrow\downarrow\rangle$, $|\downarrow\uparrow\rangle$, and $|\downarrow\downarrow\rangle$. In Fig. 11, we show that the coherent oscillations are indeed mostly between the two low-energy configurations for strong magnetic couplings. For strong ferromagnetic coupling with $M_{12} = -2$ pH, the coherent oscillations occur between $|\uparrow\uparrow\rangle$ and $|\downarrow\downarrow\rangle$, whereas the coherent oscillations occur between $|\uparrow\downarrow\rangle$ and $|\downarrow\uparrow\rangle$ for strong antiferromagnetic coupling with $M_{12} = 2$ pH.

APPENDIX E: COHERENCE

The phase coherence time T_2 between the energy eigenstates of each qubit can be characterized by measuring single-qubit coherent oscillations. As in Eq. (A21), at zero bias we define the computational basis as $|\uparrow\rangle = (|\chi_1\rangle + |\chi_2\rangle)/\sqrt{2}$ and $|\downarrow\rangle = (|\chi_1\rangle - |\chi_2\rangle)/\sqrt{2}$ for each qubit. In Fig. 12, we show the coherent oscillations of qubit 1 at $\Delta_1 = 2$ GHz. A fit to the decay envelope of the oscillations yields $T_2 = 16.2$ ns. The energy relaxation time T_1 at the same operation point is characterized by measuring the qubit excited-state population versus the delay time between initialization and readout. By fitting the excited-state population decay to an exponential function, we extract $T_1 = 17.5$ ns. We perform the same characterization on qubit 2 and obtain $T_2 = 14.3$ ns and $T_1 = 17.4$ ns at $\Delta_2 = 2$ GHz. We also fabricated uncoupled qubits with the same parameters and observed the same coherence parameters, confirming that the capacitive coupling does not degrade qubit coherence.

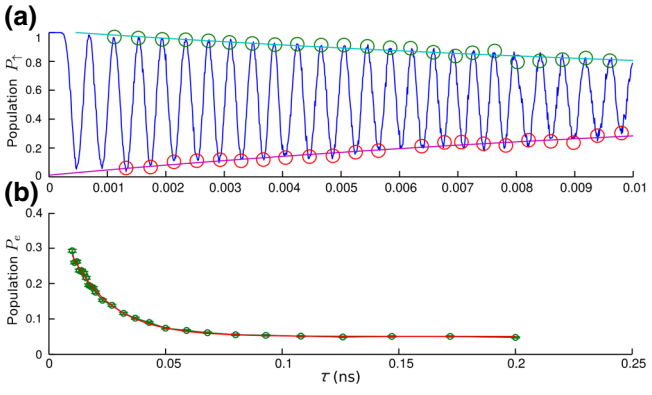

FIG. 12. T_1 and T_2 measurements on qubit 1 at $\Delta = 2$ GHz and at zero bias, $h_1 = 0$. (a) By fitting the decay envelope of the coherent oscillation to an exponential function, we obtain $T_2 = 16.2$ ns. (b) By fitting the energy relaxation of the first excited state, we obtain $T_1 = 17.5$ ns.

[1] M. W. Johnson *et al.*, Quantum annealing with manufactured spins, Nature **473**, 194 (2011).

[2] T. Kadowaki and H. Nishimori, Quantum annealing in the transverse Ising model, Phys. Rev. E **58**, 5355 (1998).

[3] E. Farhi, J. Goldstone, S. Gutmann, J. Lapan, A. Lundgren, and D. Preda, A quantum adiabatic evolution algorithm applied to random instances of an NP-complete problem, Science **292**, 472 (2001).

[4] G. E. Santoro, R. Martonak, E. Tosatti, and R. Car, Theory of quantum annealing of an Ising spin glass, Science **295**, 2427 (2002).

[5] R. Harris *et al.*, Phase transitions in a programmable quantum spin glass simulator, Science **361**, 162 (2018).

[6] A. D. King *et al.*, Observation of topological phenomena in a programmable lattice of 1,800 qubits, Nature **560**, 456 (2018).

[7] A. Mott, J. Job, J.-R. Vlimant, D. Lidar, and M. Spiropulu, Solving a Higgs optimization problem with quantum annealing for machine learning, Nature **550**, 375 (2017).

[8] M. H. Amin, E. Andriyash, J. Rolfe, B. Kulchytskyy, and R. Melko, Quantum Boltzmann Machine, Phys. Rev. X **8**, 021050 (2018).

[9] R. Harris, J. Johansson, A. J. Berkley, M. W. Johnson, T. Lanting, Siyuan Han, P. Bunyk, E. Ladizinsky, T. Oh, I. Perminov, E. Tolkacheva, S. Uchaikin, E. M. Chapple, C. Enderud, C. Rich, M. Thom, J. Wang, B. Wilson, and G. Rose, Experimental demonstration of a robust and scalable flux qubit, Phys. Rev. B **81**, 134510 (2010).

[10] R. Harris, T. Lanting, A. J. Berkley, J. Johansson, M. W. Johnson, P. Bunyk, E. Ladizinsky, N. Ladizinsky, T. Oh, and S. Han, Compound Josephson-junction coupler for flux qubits with minimal crosstalk, Phys. Rev. B **80**, 052506 (2009).

[11] S. Bravyi, D. P. DiVincenzo, R. I. Oliveira, and B. M. Terhal, The complexity of stoquastic local Hamiltonian problems, Quantum Inf. Comput. **8**, 0361 (2008).

[12] M. Marvian, D. A. Lidar, and I. Hen, On the computational complexity of curing non-stoquastic Hamiltonians, Nat. Commun. **10**, 1571 (2019).

[13] J. Klassen and B. M. Terhal, Two-local qubit Hamiltonians: When are they stoquastic? Quantum **3**, 139 (2019).

[14] E. Y. Loh, J. E. Gubernatis, R. T. Scalettar, S. R. White, D. J. Scalapino, and R. L. Sugar, Sign problem in the numerical simulation of many-electron systems, Phys. Rev. B **41**, 9301 (1990).

[15] S. V. Isakov, G. Mazzola, V. N. Smelyanskiy, Z. Jiang, S. Boixo, H. Neven, and M. Troyer, Understanding Quantum Tunneling through Quantum Monte Carlo Simulations, Phys. Rev. Lett. **117**, 180402 (2016).
[16] E. Andriyash and M. H. Amin, Can quantum Monte Carlo simulate quantum annealing? arXiv:1703.09277 (2017).
[17] T. Albash and D. A. Lidar, Demonstration of a Scaling Advantage for a Quantum Annealer Over Simulated Annealing, Phys. Rev. X **8**, 031016 (2018).
[18] L. Hormozi, E. W. Brown, G. Carleo, and M. Troyer, Nonstoquastic Hamiltonians and quantum annealing of an Ising spin glass, Phys. Rev. B **95**, 184416 (2017).
[19] H. Nishimori and K. Takada, Exponential enhancement of the efficiency of quantum annealing by nonstoquastic Hamiltonians, Front. ICT **4**, 2 (2017).
[20] R. Babbush, P. J. Love, and A. Aspuru-Guzik, Adiabatic quantum simulation of quantum chemistry, Sci. Rep. **4**, 6603 (2014).
[21] D. Aharonov, W. van Dam, J. Kempe, Z. Landau, S. Lloyd, and O. Regev, Adiabatic quantum computation is equivalent to standard quantum computation, SIAM J. Comput. **37**, 166 (2007).
[22] J. D. Biamonte and P. J. Love, Realizable Hamiltonians for universal adiabatic quantum computers, Phys. Rev. A **78**, 012352 (2008).
[23] S. P. Jordan, D. Gosset, and P. J. Love, Quantum-Merlin-Arthur-complete problems for stoquastic Hamiltonians and Markov matrices, Phys. Rev. A **81**, 032331 (2010).
[24] M. Marvian and D. Lidar, Error Suppression for Hamiltonian-Based Quantum Computation Using Subsystem Codes, Phys. Rev. Lett. **118**, 030504 (2017).
[25] Z. Jiang and E. Rieffel, Non-commuting two-local Hamiltonians for quantum error suppression, Quantum Inf. Process. **16**, 89 (2017).
[26] W. Vinci and D. A. Lidar, Nonstoquastic Hamiltonians in quantum annealing via geometric phases, npj Quantum Inf. **3**, 38 (2017).
[27] L. S. Levitov, T. P. Orlando, J. B. Majer, and J. E. Mooij, Quantum spin chains and Majorana states in arrays of coupled qubits, arXiv:0108266 [cond-mat.mes-hall] (2001).
[28] A. Lyakhov and C. Bruder, Quantum state transfer in arrays of flux qubits, New J. Phys. **7**, 181 (2005).
[29] T. Satoh, Y. Matsuzaki, K. Kakuyanagi, K. Semba, H. Yamaguchi, and S. Saito, Ising interaction between capacitively-coupled superconducting flux qubits, arXiv:1501.07739 [quant-ph] (2015).
[30] A. J. Kerman, Superconducting qubit circuit emulation of a vector spin-1/2, New J. Phys. **21**, 073030 (2019).
[31] F. Yan, P. Krantz, Y. Sung, M. Kjaergaard, D. L. Campbell, T. P. Orlando, S. Gustavsson, and W. D. Oliver, Tunable Coupling Scheme for Implementing High-Fidelity Two-Qubit Gates, Phys. Rev. Appl. **10**, 054062 (2018).
[32] M. Kounalakis, C. Dickel, A. Bruno, N. K. Langford, and G. A. Steele, Tuneable hopping and nonlinear cross-Kerr interactions in a high-coherence superconducting circuit, npj Quantum Inf. **4**, 38 (2018).
[33] J. D. Whittaker *et al.*, A frequency and sensitivity tunable microresonator array for high-speed quantum processor readout, J. Appl. Phys. **119**, 014506 (2016).
[34] A. J. Berkley, M. W. Johnson, P. Bunyk, R. Harris, J. Johansson, T. Lanting, E. Ladizinsky, T. Tolkacheva, M. H. S. Amin, and G. Rose, A scalable readout system for a superconducting adiabatic quantum optimization system, Supercond. Sci. Technol. **23**, 105014 (2010).
[35] C. M. Quintana *et al.*, Observation of Classical-Quantum Crossover of 1/f Flux Noise and its Paramagnetic Temperature Dependence, Phys. Rev. Lett. **118**, 057702 (2017).
[36] Although the capacitive coupling is off, the capacitive loading on the individual qubits is kept in the simulation.
[37] M. H. Amin, A. Yu. Smirnov, N. G. Dickson, and M. Drew-Brook, Approximate diagonalization method for large-scale Hamiltonians, Phys. Rev. A **86**, 052314 (2012).